Nanoscale

PAPER

View Article Online
View Journal

Cite this: DOI: 10.1039/c7nr03847j

Tumor-targeted nanoprobes for enhanced multimodal imaging and synergistic photothermal therapy: core–shell and dumbbell Gd-tailored gold nanorods†

Jinchang Yin, [a] Deqi Chen,[a] Shuangshuang Wu,[a] Chaorui Li,[a] Lizhi Liu[b] and Yuanzhi Shao *[a]

Multifunctional nanoprobes, due to their unique nanocomposite structures, have prominent advantages that combine multimodal imaging of a tumor with photothermal therapy. However, they remain a challenge for constructing nanostructures *via* conventional approaches due to the peculiar environmental sensitivity of each component. Here, we report the design and synthesis of Gd-based nanoparticle-tailored gold nanorods with distinctive core–shell and dumbbell nanoarchitectures (NAs) by a specific synthesis technology. The prepared NAs possess a tunable particle size of 80–120 nm in length and 50–90 nm in diameter, which are suitable for cellular uptake and passive targeting of a tumor. The formation of two distinct heterostructures and their underlying mechanism were studied through systematic investigations on the controllable synthesis process. The as-prepared nanoprobes possess an ultrahigh longitudinal relaxivity (r_1) of 22.69 s^{-1} mM^{-1} and thus a significant magnetic resonance imaging signal enhancement has been observed in mice tumors. The NAs, especially the dumbbell type, show a vivid two-photon cell imaging and a remarkable photothermal conversion efficiency owing to their superior longitudinal surface plasmon resonance. Both *in vitro* cytotoxicity and *in vivo* immunotoxicity assays give substantial evidence of excellent biocompatibility attained in the NAs. The development of multifunctional targeting nanoprobes in this study could provide guidance for tailored design and controllable synthesis of hetero-structured nanocomposites utilized for multimodal imaging and photothermal therapy of cancer.

Received 31st May 2017,
Accepted 22nd July 2017

DOI: 10.1039/c7nr03847j

rsc.li/nanoscale

Introduction

Noble gold nanoparticles (AuNPs) have been of considerable research interest in biomedical fields due to their unique optical properties and excellent biocompatibility.[1] Compared with common sphere noble AuNPs, anisotropic gold nanorods exhibit a stronger surface plasmon resonance (SPR) which is related to the length-to-diameter aspect ratio (AR).[2] The SPR peak of gold nanorods can be shifted from visible regions (550 nm) to near-infrared regions (1550 nm) by tuning the aspect ratio.[3] Intensive absorption and scattering at two optically transparent windows[4] for biological tissues and continually regulatable photothermal conversion efficiency make gold nanorods qualify as an ideal system for optical imaging and photothermal therapy.[5] Gold nanorods could be facilely modified and readily combined with other materials,[6,7] forming various structures with more intriguingly physical, chemical and biological properties, as well as serving multimodal imaging diagnosis and cancer therapy.[8,9]

Multimodal imaging is a new approach for molecular imaging, and it overcomes the limitations of single modal imaging in disease diagnosis.[10] For instance, magnetic resonance imaging (MRI) is a noninvasive technique with excellent accuracy in spatial resolution, and it provides high-resolution anatomic information about tissues and their orientation as well as quantitative analysis of the image features of deep tissues.[11] However, due to its limited sensitivity, MRI can merely detect molecular changes from mmol to μmol in low sensitivity.[12] Meanwhile, an optical imaging technique exhibits

[a]*School of Physics, State Key Laboratory of Optoelectronic Materials and Technologies, Sun Yat-sen University, Guangzhou 510275, P. R. China. E-mail: stssyz@mail.sysu.edu.cn*

[b]*State Key Laboratory of Oncology in Southern China, Imaging Diagnosis and Interventional Center, Cancer Center, Sun Yat-sen University, Guangzhou 510060, P. R. China*

†Electronic supplementary information (ESI) available: Size distribution histograms and the corresponding TEM images of gold nanorods, CSNAs and DBNAs; DLS; FTIR; XRD; EDX spectra; XPS; EELS-EFTEM; extinction spectra and the corresponding TEM images; room temperature magnetization curves; X-band EPR spectra; *in vivo* MR images; photothermal conversion efficiency calculation; CompuCell3D simulation; cell cycle analysis; the origin apoptosis data. See DOI: 10.1039/C7NR03847J

sensitivity at the single molecule level and rapid response time (ps) but suffers from a low spatial resolution.[10,13] Therefore, a single modal imaging technique cannot meet the demand in diagnosing diseases. A multimodal imaging approach that combines the high spatial resolution of MRI and high sensitivity of optical imaging serves as an ideal imaging technique.[14,15]

The key point to integrate each imaging mode is the design of multimodal nanoprobes.[16,17] The Gd^{3+} complex has been widely used as a T_1-weighted contrast agent (CA) for enhanced MRI, due to its high spin magnetic moment and long electron spin relaxation time.[14,18] Nanoparticulate gadolinium-based CAs, as compared to gadolinium chelate CAs used in clinical MRI, exhibit higher relaxivity and longer blood circulation life.[19] Because of their enhanced permeation and retention effect, this class of particulate agents can play a passive role in targeting the tumor tissues.[19–21] For gold nanorods, the probability of radiative inter-band transition can be improved by the longitudinal SPR effect along the long axis, which makes it possible to emit fluorescence *via* a two-photon process. Furthermore, a weaker damping in the localized surface plasmon resonance induced by rod-shaped gold nanoparticles can lead to a stronger enhancement of field effect than that of spheroidal gold nanoparticles.[2,22] Near-infrared light is usually employed as a laser source for two-photon-excited luminescence (TPL) imaging. Because of the low tissue photodamage, less background auto-fluorescence and high penetration capability (>500 μm), TPL imaging has appeared as the most promising fluorescence technique.[2–4,23] Apart from two-photon imaging, gold nanorods can be utilized as CAs for surface-enhanced Raman scattering (SERS)[24–26] imaging, X-ray computed tomography (X-CT)[26,27] and photoacoustic (PA)[28] imaging.[30–35] A combination of Gd-based nanoparticles with Au nanorods is a very effective method for multimodal imaging. However, the combinative approach reported in previous investigations is simply the integration of gold nanoparticles with Gd^{3+} chelates.[21,29–31] In our previous work, we investigated a nanocomposite formed by simply mixing gold nanospheres and gadolinium oxide nanoparticles using an organic element that would be very likely to separate in a living body; the relative amounts of Gd and Au in each nanoparticle were hardly determined in humans.[32,33] The well-known Gd-based nanoparticle precipitation reaction occurs at an elevated temperature under agitation.[34–36] However, under vigorous conditions, some gold nanorods were readily transformed into nanospheres.[37,38] Besides, the precipitation cannot proceed due to the peculiar environmental sensitivity and incongruous surface of both components. Here, we propose a new design strategy to fabricate two distinct Gd-tailored gold nanorods that can take full advantage of them both for two-photon and magnetic resonance imaging. Owing to their high efficiency of photothermal conversion and excitation by near infrared light, gold nanorods can be applied not only for imaging diagnosis but also for photothermal therapy (PTT) and photodynamic therapy (PDT).[5,22,39] Because cancer cells are very sensitive to high temperatures (>42 °C), the adjustable hyperthermia effect of gold nanorods can also be adopted in the treatment of cancer with a proper NIR laser to destroy tumor cells.[40,41]

In the present work, we have developed a novel multistep scenario to fabricate PEGylated Gd-tailored gold nanorods in two peculiar shapes of core–shell and dumbbell nanoarchitectures. This is, to the best of our knowledge, the first report to coalesce Gd-based nanoparticles and gold nanorods into these two distinct forms of nanocomposites. The morphology, structure, size and compositions of the two forms of the NAs were then examined thoroughly. To gain an insight into the underlying mechanism for two well-formed core–shell and dumbbell NAs with a suitable size,[21,34–36,42] a set of experiments controlling accurately the synthesis process and raw reagents were conducted following the *ad hoc* transmission electron microscopy (TEM) observations of the prepared nanocomposites. Furthermore, we measured the magnetic and optical properties of the NAs, and performed TPL imaging, PTT assays in HeLa cells as well as MR imaging of tumor mice. We also systematically performed *in vitro* cytotoxicity and *in vivo* immunotoxicity assays for validating the safety of both NAs. Other details concerning the results can be found in the ESI (Fig. S1–S24, eqn (S1)†).

Results and discussion

Synthesis and characterization of core–shell Gd-tailored AuNRs

Typical core–shell structured AuNR@SiO_2@$Gd_2O(CO_3)_2$ nanoarchitectures (CSNAs) were prepared by a facile urea-based homogeneous coprecipitation approach. The gold nanorods coated with ultrathin silica layers were deposited by gadolinium oxide carbonate shells at a standard temperature of 80 °C for 3–5 h. The CSNAs coated with nanoshells of various thicknesses could be achieved by simply changing the amounts of raw reagents, *e.g.* gadolinium nitrate hexahydrate.

The TEM observation at low magnifications (Fig. 1a) shows that the CSNAs are well dispersed and are of uniform nanostructures with nearly 100% core–shell and rod-shaped yield. The TEM images at middle magnifications (Fig. 1b and c) also demonstrate clear and well-formed core–shell structures with two different shell thicknesses. The thin CSNAs are around 98.8 nm in length and 53.4 nm in diameter, whereas the thick CSNAs are around 120.1 nm in length and 68.5 nm in diameter under the condition of close sizes of AuNR cores (Fig. S1†). Moreover, dynamic light scanning (DLS) spectra (Fig. S2†) indicate that the hydrodynamic sizes of the CSNAs with thin and thick shells dispersed in aqueous solutions are about 123 nm and 157 nm, respectively. The average sizes are slightly larger than those observed under TEM due to the presence of polyethylene glycol (PEG) as the surfactant coating the particle. PEG molecules and the hydration of PEG shells in water are also calculated as part of the hydrodynamic diameter. Usually, PEG is used for improving the biocompatibility of the synthesized CSNAs and prolonging the circulation life in the blood as well as facilitating the effective passively-

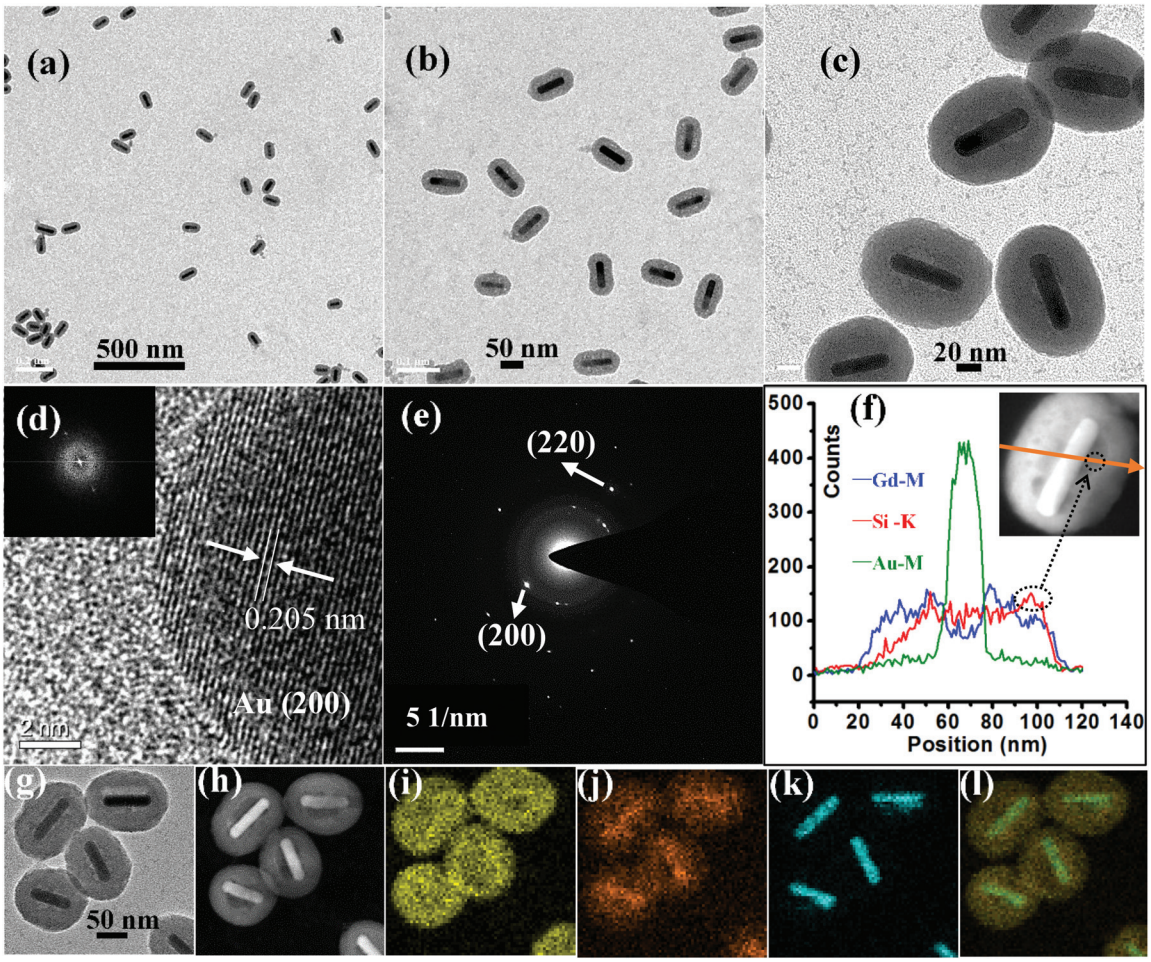

Fig. 1 Typical TEM images of core–shell PEGylated AuNR@SiO_2@$Gd_2O(CO_3)_2$ NAs with thin (a, b) and thick (c, d) shells at low (a), middle (b, c) and high (d) magnifications. The inset in (d) is the related fast Fourier transform (FFT) pattern. (e) The corresponding SAED pattern of the NAs. (f) EDX line-scanning profiles analyzed across an entire particle body as shown by the arrow in the inset of the HAADF-STEM image. (g) TEM image, (h) HAADF-STEM image of the used NAs for the corresponding EDX elemental mapping images of elements Gd (i), Si (j), Au (k) and the mixture (l) of the three elements.

targeted accumulation in tumors. The successful encapsulation of PEG in this study could be verified by Fourier transmission infrared (FTIR) spectra (Fig. S3†).

High-resolution TEM (HRTEM) and selected area electron diffraction (SAED) analysis (Fig. 1d and e) show that the CSNAs consist of both face-centered cubic phase single crystals of Au (PDF # 04-0784) and the amorphous phase of shells. The lattice interplanar spacing was figured out as 0.205 nm, which corresponds to the (200) plane of the Au crystalline structure. The amorphous phases were determined as SiO_2 and $Gd_2O(CO_3)_2$, further supported by powder X-ray diffraction (XRD, Fig. S4†). Energy-dispersive X-ray (EDX) line scanning and elemental mapping analysis (Fig. 1f–l) trace the distributions of Gd, Si and Au elements graphically. Au and Gd elements are segregated mainly in the inner core and outer layer regions, whereas the Si element is situated in the interlayer and slightly close to the gold nanorod core. However, the profile between the outer layer and interlayer is vague. The darker concave near the bright gold nanorod shows up noticeably only in high-angle annular dark-field scanning TEM (HAADF-STEM) shown in Fig. 1h and the inset of Fig. 1f, and is verified as silica according to the line scanning of the Si element. By controlling the synthesis process, we could achieve a visibly clear core-interlayer–outermost layer structure (Fig. S5a†). However, a thick silica layer (Fig. S5b†) might enlarge the particle size and obstruct the interaction and the electronic coupling between Gd^{3+} ions and gold nanorods, which will be further investigated in future. The molar ratios of Gd, Si and Au in the as-prepared CSNAs with thin and thick shells are about 8 : 1 : 2 and 16 : 1 : 2, respectively, in accordance with the energy dispersive X-ray spectroscopy (EDX) analyses (Fig. S6†). To further unveil the chemical state and the interaction of each element, we performed X-ray photoelectron spectroscopy (XPS) analyses as shown in Fig. S7.† The gold (Au 4f) signal is not significantly detected because of the thicker shell definitively more than the XPS sampling depth.[43] The Si 2p peak can be deconvoluted into two bands: one arises from the Si–O–Si siloxane bonds of the silica structure (103.0 eV); the other is attributed

to the formation of Si–O–Gd bonds (101.9 eV). These line shapes and peak positions can be compared with earlier published data[44,45] to confirm the bonding of silica with gadolinium. The C 1s peak at 289.7 eV can be assigned to the carbon atoms in carbonate (CO_3^{2-}).[46]

Synthesis and characterization of dumbbell Gd-tailored AuNRs

Dumbbell-shaped AuNR@SiO_2@$Gd_2O(CO_3)_2$ nanoarchitectures (DBNAs) were prepared using the same coprecipitation method and original gold nanorods (Fig. 2a) but with a different precursor. The precursor AuNR@SiO_2 nanocomposites (Fig. 2b) exhibit clear and special dumbbell heterostructures. The dumbbell-like geometry is dissimilar to its core–shell counterpart, and it results from the different dosage of cetyltrimethylammonium bromide (CTAB) that modifies the surface of gold nanorods. In hot alkaline solution, the AuNR@SiO_2@$Gd_2O(CO_3)_2$ dumbbell nanoarchitectures (Fig. 2c and Fig. S8†) were formed by decomposing and reshaping the precursors. The DBNAs having a length of around 88.6 nm and an end diameter of 36.6 nm, shrunk apparently in comparison with those of their precursors (length of about 107.2 nm and end diameter of 58.3 nm) in Fig. S9.† The hydrodynamic diameter of the PEGylated DBNAs in aqueous solution determined by DLS size distribution is about 112 nm (Fig. S10†).

HR-TEM and SAED (Fig. 2d and e) detect the presence of a single crystal phase of the Au nanorod core with an interplanar spacing of 0.203 nm from the (200) plane, which is well consistent with those obtained from XRD measurements (Fig. S11†). The locations of Gd, O, Si and Au elements are displayed by using the EDX line scanning and elemental mapping of the DBNAs (Fig. 2f–n). The analysis of XRD and elemental mapping could validate the existence of the

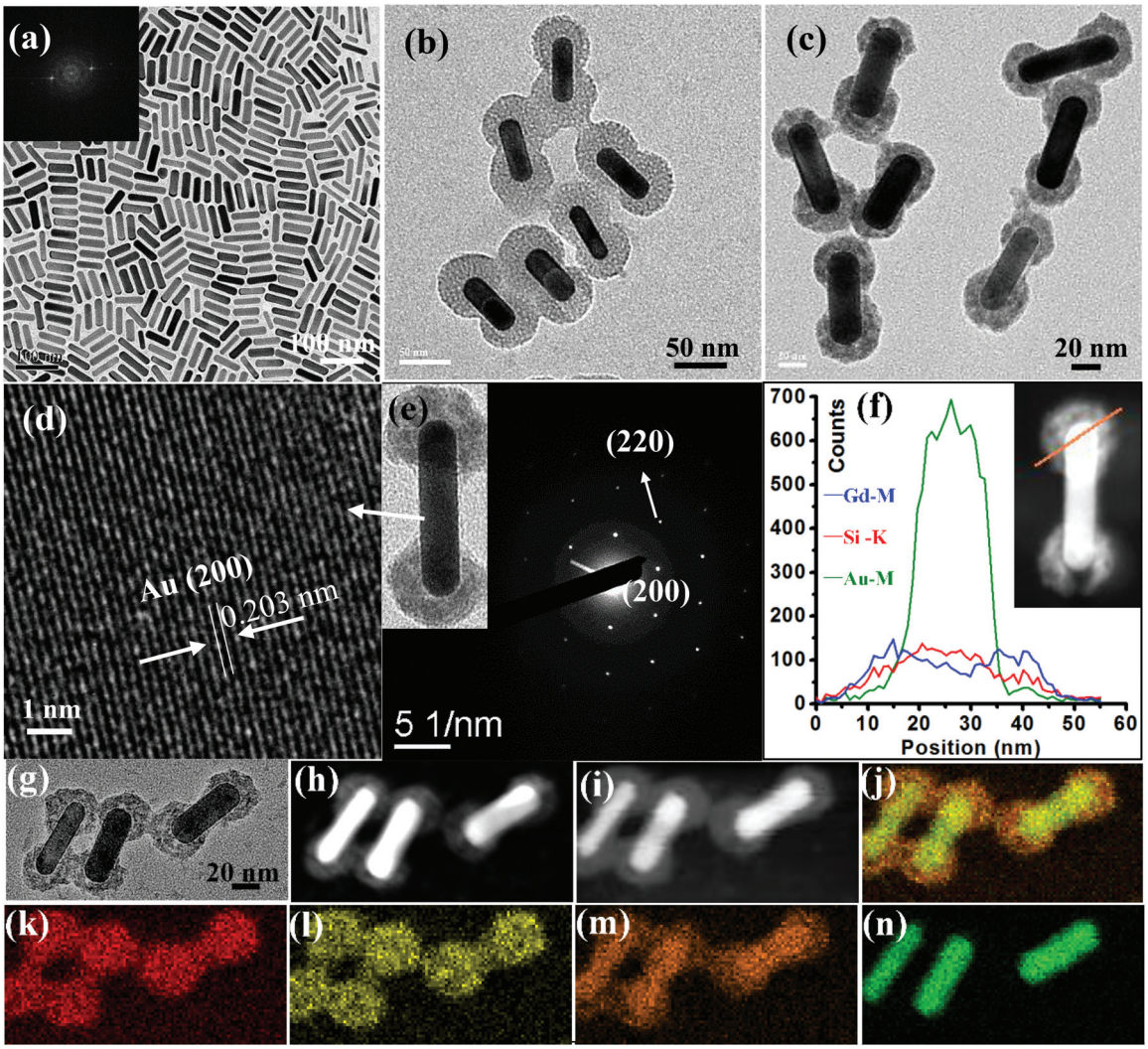

Fig. 2 (a) Broad-view TEM image of typical gold nanorods with the inset FFT of a gold nanorod particle. (b, c) TEM images of the precursor AuNR@SiO_2 DBNAs and the final AuNR@SiO_2@$Gd_2O(CO_3)_2$ DBNAs. (d) HR-TEM image and (e) SAED pattern of an individual with the well-formed dumbbell heterostructure shown as the inset image. (f) EDX line-scanning profiles analyzed across the end spherical region as viewed along the line in the inset of the HAADF-STEM image. (g) TEM image, (h, i) STEM images before and after EDX mapping of the NAs. (j) The corresponding elemental mixed mapping images of elements O (k), Gd (l), Si (m) and Au (n).

amorphous phase shell of SiO_2 and $Gd_2O(CO_3)_2$. The detailed Gd, Si, Au composition analyses from the precursor to the final NAs using EDX spectra (Fig. S12†) display the decrease of the Si content and the increase of the Gd content. The molar ratio of Gd, Si, Au in the DBNAs is 1.3 : 1 : 6.4, exhibiting the evident discrepancy between the DBNAs and the CSNAs (Fig. S6†). To further prove the element carbon (C) acting as one component in the presence of the shell, we replaced the carbon film with the micro grid film and measured the electron energy loss spectroscopy-energy filtering TEM (EELS-EFTEM) element mapping of the NAs without PEG encapsulation in the hole of the micro grid film. The mapping of carbon is close to that of gadolinium (Fig. S13†), indicating that the C element exists in the shell of the DBNAs and the materials of the shell are indeed gadolinium oxide carbonates. The XPS data (Fig. S14†) show two significant Au 4f peaks at 87.4 eV and 84.0 eV, which are ascribed to the surface Au^{3+} and Au^0 species of the exposed gold nanorods.[47] The chemical nature of the shell including Gd, Si and C species in DBNAs is similar to that in CSNAs.

Formation mechanism

The well-formed gold nanorods were fabricated using a seed-mediated, surfactant-assisted growth by a two-step method. CTAB was used as the surfactant to stabilize colloidal Au nanorods. It is difficult to directly deposit Gd-based nanoparticles on the surface of AuNRs or CTAB-coated AuNRs *via* urea-based coprecipitation. Gold nanorods would be deformed under these vigorous and tough precipitating conditions, meanwhile, Gd^{3+} ions would be solely formed as large gadolinium oxide carbonate microparticles instead of depositing onto gold nanorods. Afterwards, silica was taken into account for its ready combination with either AuNRs or Gd-based nanoparticles. Because of the electrostatic interaction between negative and positive ions, rare-earth Gd^{3+} cations are extremely easily bound to the oxygen-rich surface of the silica, which causes a slow growth under homogeneous conditions.

The entire synthetic procedures and formation mechanisms of both CSNAs and DBNAs (Fig. 3a) are mainly divided into two parts, namely, coating of SiO_2 on AuNRs and depositing $Gd_2O(CO_3)_2$ onto AuNR@SiO_2 NAs. There are two crucial points: 1. how to construct a AuNR@SiO_2 dumbbell nanoarchitecture, which is quite different from core–shell NAs; 2. the finally-yielded AuNR@SiO_2@$Gd_2O(CO_3)_2$ NAs derived from their precursor AuNR@SiO_2 NAs are smaller in particle size than or close to that of the precursors. In the first reaction, CTAB, employed as the structure-directing agent, plays a key role in constructing the core–shell and dumbbell AuNR@SiO_2 NAs. In the absence or with traces of CTAB, the well-formed core–shell structure was fabricated under mild synthetic conditions. The fascinating dumbbell AuNR@SiO_2 NAs were obtained after adding 10 mg CTAB, owing to the molecular packing state of CTAB beside two sides of Au nanocrystals, which can completely inhibit the silica deposition in the transverse direction in comparison with the longitudinal [100] direction. The selective deposition of silica on the end surface is preferably realized by coating the gold nanorod sides with CTAB molecules. The reactions at two ends and sides of single-crystal gold rods are different from each other. The interaction between the surface-capped CTAB and the {110} facets is stronger than {111} facets. Thus, CTAB bilayers are more compact at the sides than at the ends of the nanorods, facilitating more silica deposited at the two ends of AuNRs and the formation of dumbbell-shaped nanostructures subsequently.

The size distributions (Fig. S9†) reveal the smaller mean sizes of the finally yielded NAs than those of the precursor NAs. It is conducive to obtaining a particle size suitable for *in vivo* biomedical application. Undoubtedly, larger particles are prone to aggregation and then blocking blood vessels, leading to the potential danger of arterial embolism. Meanwhile, ultrasmall particles can pass through the intact blood–brain barrier and might accumulate in healthy brain, posing potential risks.[21,35,36] Therefore, tuning the variation of the particle sizes is extremely significant and considerable. To understand the formation mechanism of AuNR@SiO_2@$Gd_2O(CO_3)_2$ NAs from AuNR@SiO_2 NAs, a set of experiments regarding the synthesis duration were conducted following TEM observations. The variations in the length and diameter of the NAs (Fig. 3b and c) exhibit the collapse of AuNR@SiO_2 core–shell nanostructures and the reconstruction of AuNR@SiO_2@$Gd_2O(CO_3)_2$ NAs. In the initial stage of reaction II, a quite large pH value ($\geq$11) is achieved due to the over-dosage of urea reagents; meanwhile, a comparatively high temperature ($\geq$80 °C) leads to the destruction of the surface amorphous silica *via* dissociating Si–O bonds. The monosilicate and polysilicate species converted by resolved silica rapidly dissolve in aqueous solution. The absorption of residual ultrathin silica close to gold nanorods makes the nanoparticles oxygen-enriched. Bicarbonate ions, once decomposed from urea, could combine with Gd^{3+} ions and then deposit on the surface of silica-modified Au nanorods. The outer layer thickness can be precisely controlled by not only the amount of gadolinium raw reagents added but also the prolonged duration. However, longer reaction times (>3 h) cannot lead to coarsening of the NAs further.

Plasmonic optical properties and intracellular TPL imaging

The unique localized surface plasmon resonance of gold nanorods has found its applications in both bioimaging diagnosis and photothermal therapy, especially for a strong long-wavelength plasmonic longitudinal absorption band originating from free electron collective oscillations along the length axis of the gold nanorods. To validate the SPR properties of both PEGylated AuNR@SiO_2@$Gd_2O(CO_3)_2$ DBNAs and CSNAs, we investigated their optical absorption with AuNR cores of the close length-to-diameter aspect ratio (Fig. 4a). Compared with pure gold nanorods, both Gd-engineered CSNAs and DBNAs exhibit a close shape of SPR bands, despite the slightly decreased longitudinal SPR peak values. The DBNAs have a more intense SPR absorption ability than that of CSNAs, which may be contributed to the shell slightly impeding the light penetration.[48] When the gold nanorod is coated with silica and gadolinium oxide carbonate nanolayers, its longitudinal

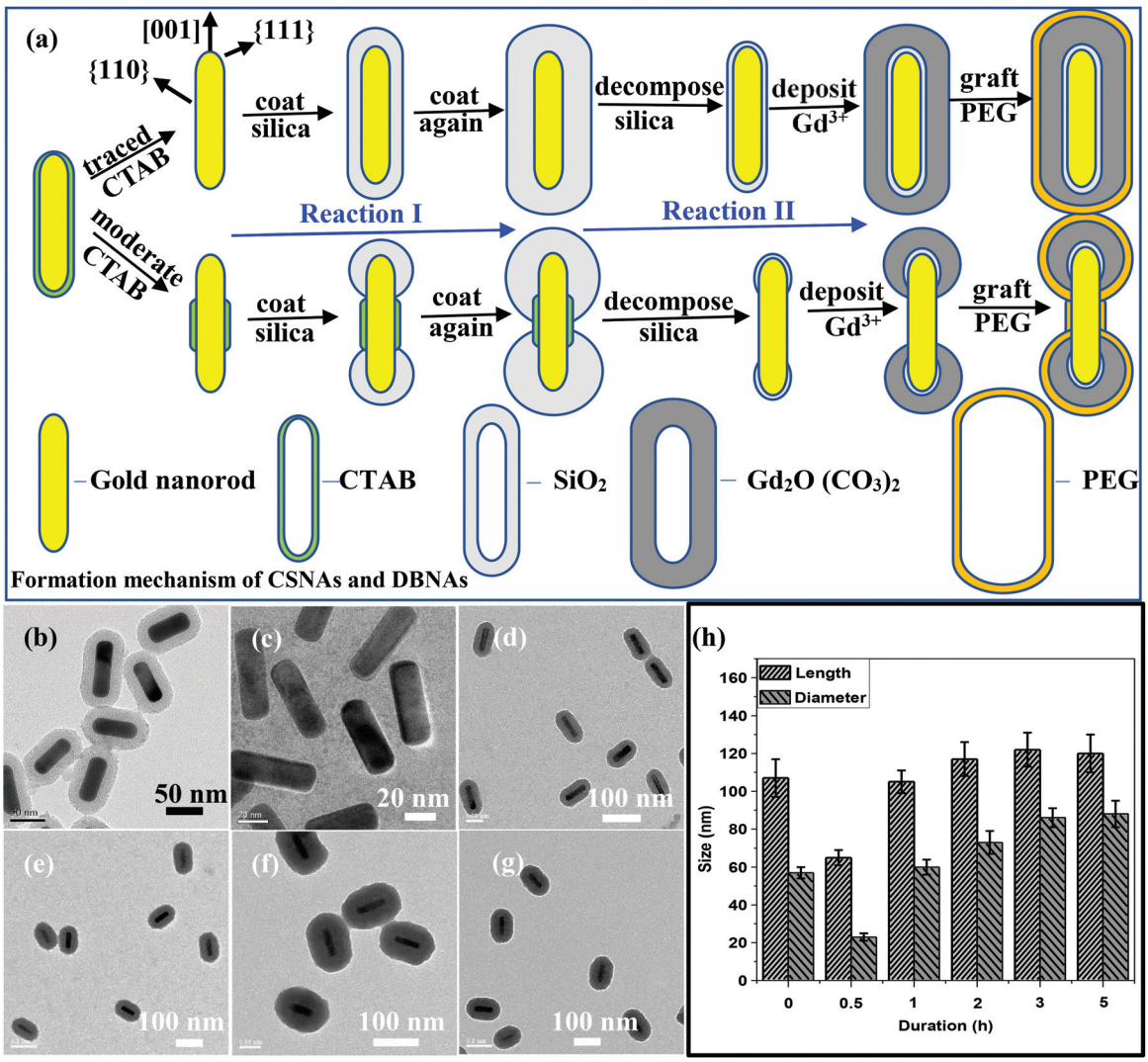

Fig. 3 (a) Schematic illustration of the formation mechanism and the fabrication procedures of the distinct core–shell and dumbbell PEGylated AuNR@SiO_2@$Gd_2O(CO_3)_2$ NAs. The gold nanorod is labeled with the {111} facet in the end, the {110} facet in the side and the [001] direction across the longitudinal axis. (b–g) Typical TEM images of the NA transformation from the precursor AuNR@SiO_2 NAs to the final AuNR@SiO_2@$Gd_2O(CO_3)_2$ NAs in reaction II with a duration of 0, 0.5, 1, 2, 3 and 5 h, respectively. (h) The length and diameter histogram of the relevant NAs regarding the different synthesis durations.

SPR bands shift to the red wavelength region due to the larger local refractive index of silica and gadolinium oxide carbonate than that of aqueous solutions around gold nanorods. In the UV-visible-NIR absorption spectra, the maximum SPR absorption of the DBNAs and CSNAs is observed at 773 and 791 nm, respectively, in comparison with the original gold nanorods with a maximum SPR absorption peak at 735 nm. The CSNAs used are the core-thin shell NAs and we employ them to the TPL and PTT assays because the CSNAs with a thick shell exhibit a relatively weak SPR absorptivity (Fig. S15†). The extinction spectra and corresponding TEM images of AuNRs, AuNR@SiO_2 NAs and AuNR@SiO_2@$Gd_2O(CO_3)_2$ NAs with two kinds of gold nanocores with aspect ratios of 3.3 and 4.2 (Fig. S16†) present the close and strong SPR absorptions of the precursors and finally yielded NAs.

Unfortunately, it is hard to detect their photoluminescent signals through a conventional Edinburgh spectrofluorophotometer system. However, by means of ultrashort laser pulses, gold nanorods could exhibit distinguished two-photon-induced luminescence due to their strong SPR frequency coupled with the extremely enhanced electromagnetic fields around their surfaces. It has been reported that the two-photon action cross-section of gold nanorods is larger than 2000 GM (1 GM = 10^{-50} cm^4 s per photon). Two-photon laser scanning confocal microscopy images of PEGylated DBNAs and CSNAs in HeLa cells (Fig. 4(b–g)) were obtained using a femtosecond Ti-sapphire oscillator (800 nm) as the excitation source and tuning the emission wavelength in the range of 620 to 700 nm. After coincubation for 2 h, remarkably visible red fluorescence images were observed in the cytoplasm of living

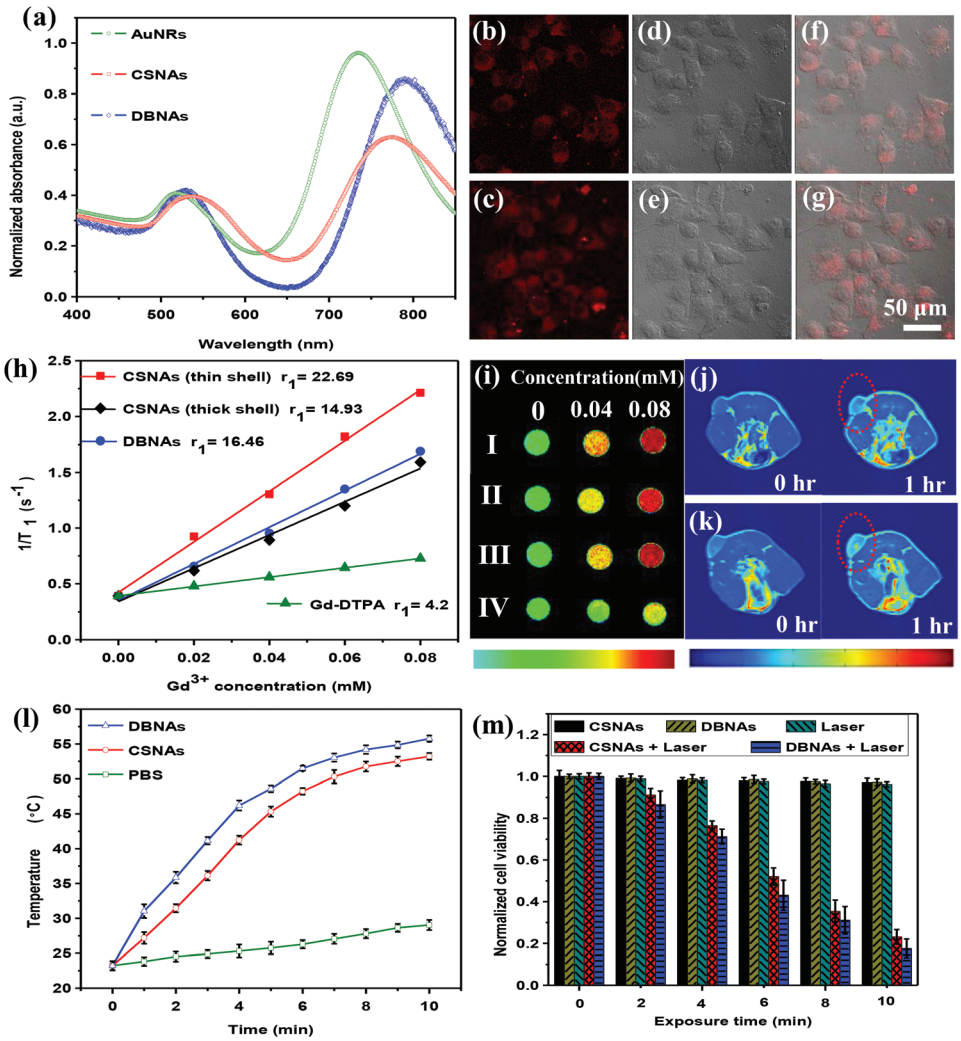

Fig. 4 (a) UV-visible-NIR spectra of AuNRs, core–shell and dumbbell NAs in water. The lines have been normalized to keep the same transverse absorption peak value. (b, c) Two-photon laser scanning confocal microscopy images, (d, e) bright-field inverted microscopy images and (f, g) the merged images of HeLa cells incubated with 20 μg mL^{-1} core–shell (b, d, f) or dumbbell (c, e, g) NAs. An 800 nm laser light was used for excitation and the image was obtained *via* tuning the emission in the red channel with a wavelength in the range of 620 to 700 nm. (h) Plots of the relaxation rate ($1/T_1$) as the linear function of Gd^{3+} concentration of the Gd-DTPA, dumbbell and core–shell NAs with a thin or thick shell. The slope is just the longitudinal relaxivity (r_1). (i) The corresponding *in vitro* T_1-weighted MR phantoms. (j, k) *In vivo* MR images of 4 T1 xenografted tumors in Balb/c nude mice (23 mg) before and after administration with 10 μmol kg^{-1} core–shell (j) or dumbbell (k) NAs into the tail vein of mice. The tumor part is labeled with the red cycle. (l) Temperature increase curves of PBS, core–shell and dumbbell NAs (0.1 μmol L^{-1} Au) in the same volume aqueous solution irradiated with a 800 nm NIR laser at 1.0 W cm^{-2}. The temperature rise as the nonlinear function of exposure times. (m) Time-dependent cell viability of HeLa cells incubated with 100 μg mL^{-1} core–shell or dumbbell NAs under laser illumination of 800 nm excitation (1.0 W cm^{-2}). The assays without any NAs or laser were conducted as the control under the same conditions.

cells, indicating the unique two-photon imaging capability and effective uptake of two kinds of the NAs. Two-photon-excited luminescence from the cores of gold nanorods has been considered as a series of steps including a sequential absorption of photons for creating a combination of an electron in the d-band and a hole in the sp-band, as well as a further relaxation of electron–hole pairs for emitting bright visible light. The first photon located in the sp conduction band below the Fermi surface creates a hole, and then the second photon excites an electron in the d-band to the hole in the sp conduction band. The clear red intracellular fluorescence and the successful internalization into tumor cells indicate that the two nanostructures can be further developed into an efficacious two-photon luminescence targeted nanoprobe for *in vivo* biolabeling and bioimaging applications.

Magnetic properties and tumor-targeted MR imaging

The paramagnetic Gd^{3+} ions in the DBNAs and CSNAs primarily contribute to the positive signal enhancement in MRI and serve as T_1-weighted contrast agents. The typical paramagnetic characteristics of PEGylated AuNR@SiO_2@$Gd_2O(CO_3)_2$ DBNAs and CSNAs at room temperature were verified by the field-

dependent magnetization curves and electron paramagnetic resonance (EPR) spectra (Fig. S17†). The broad EPR spectra disclose a strongly coupled spin interaction of paramagnetic Gd^{3+} ions, which is expected to increase the water proton spin–lattice T_1 relaxation surrounding Gd^{3+} ions. To assess the relaxation properties of the NAs, the longitudinal relaxation times in various Gd^{3+} concentrations were obtained utilizing a 0.55 T Mini-MR system (Fig. 4h). The Gd^{3+} concentrations of all samples were quantified by the inductively coupled plasma mass spectroscopy (ICP-MS). The relaxivity values of the CSNAs with a thin or thick shell and the DBNAs were measured to be nearly 5 times as large as that of the commercial MR contrast agent Gd-DTPA. The thin shell CSNAs possess a higher relaxivity in comparison with the thick shell CSNAs because of the larger specific ratio of specific surface to shell volume.[36,49,50] *In vitro* MRI pseudo color pictures of the NAs (Fig. 4i) imaged by a 0.5 T clinical MRI system reveal a much brighter color than that of Gd-DTPA in the same Gd concentration. We also performed *in vivo* T_1-weighted MR imaging of the 4T1 subcutaneously-xenografted tumor mice with intravenous administration of 10 μmol kg^{-1} core–shell (Fig. 4j and Fig. S18a–e†) or dumbbell NAs (Fig. 4k and Fig. S18f–j†). After 1 h, an observable signal enhancement appears in tumors *via* passively targeted accumulation, signifying the feasibility of applying both NAs as tumor-targeted CAs. It is noteworthy that the quantified Gd^{3+} concentration utilized in the MRI assessment is about 1/15 of a clinically-used standard Gd-DTPA dose (0.1–0.2 mmol kg^{-1}). Overall, both *in vitro* and *in vivo* T_1-weighted MRI results disclose that the core–shell and dumbbell PEGylated NAs are potential candidates as targeting nanoprobes for cancer imaging diagnosis.

In vitro PTT performance

A gold nanorod exhibits an excellent photothermal conversion efficiency because of its intense longitudinal SPR bands extending to the near-infrared regions, which can be employed for hyperthermia tumor therapy under the irradiation of a near-infrared continuous-wave laser. The photothermal conversion properties of both CSNAs and DBNAs with maximum plasmonic absorbance around 800 nm were explored using 800 nm irradiation with a low laser power density of 1.0 W cm^{-2} for 10 min (Fig. 4l). Compared with a temperature rise of 29.04 °C in the irradiated PBS buffer solutions, the temperature of the DBNAs in PBS solutions rapidly reached the highest at 55.77 °C, and the temperature for the CSNA mixtures was 53.22 °C. Even for a duration of 4 min, the temperature could rise to 46.20 °C. The temperature rising rate reaches almost 11 °C min^{-1}, displaying a good photothermal conversion rate at first 4 min. After 6 min, the temperature rising rate decreases to less than 1 °C min^{-1}, conducive to avoiding a superheated damage to normal organs. The photothermal conversion efficiencies of CSNAs and DBNAs have been calculated as 17.2% and 20.6%, respectively (eqn (S1)†), which are close to the reported Au nanorods (21%).[51] After 10 min of exposure, both CSNAs and DBNAs retain the original structure and morphology (Fig. S19†) as well as the unchanged SPR absorption intensity (Fig. S20†), indicating an excellent photothermal stability. To further evaluate the PTT efficacy of the as-synthesized NAs, a series of experiments based on the photothermal killing of cancer cells were conducted using a NIR laser with 1.0 W cm^{-2} power and tested *via* CCK8-based cell viability assays. According to the results of the CCK8 tests (Fig. 4m), less than 3% of HeLa cells were dead in the absence of the DBNAs, CSNAs or lasers after 10 min of the PTT experiment, whereas about 80% of HeLa cells were dead in the presence of the therapeutic NAs under a continuous 800 nm laser irradiation for 10 min. The efficient photothermal killing of the cervical carcinoma HeLa cells observed in the case of both DBNAs and CSNAs render them an eligible nanotheranostic candidate for cancer therapy in clinical application. To further evaluate the effect of thermal treatment on inhibiting tumor growth, we took advantage of a well-known modelling software package, CompuCell3D,[52,53] to simulate the spatiotemporal variation of a tumor subjected to evaluated temperatures. *In silico* tumor growth models as well as the dynamic curves at ambient and evaluated temperatures qualitatively demonstrate that the heat indeed inhibits angiogenesis and prevents tumor growth (Fig. S21 and S22†).

Toxicity assays

Due to the toxic CTAB included in the synthesis of gold nanorods and the possibility of Gd^{3+} ions dissociating from the nanoparticles, evaluating the preliminary *in vitro* and *in vivo* toxicity is particularly important and a prerequisite for clinical bioapplications. CTAB was principally extracted *via* repeatedly washing gold nanorods with NH_4NO_3 solution, hot acid ethanol and deionized water in the first synthesis step. In the second step, it can be removed thoroughly owing to the high temperature of 80 °C and vigorous stirring. The successful CTAB elimination can be verified by FTIR (Fig. S3a–c†), which could be justified from the nearly vanished C–H bonds shown in Fig. S3b.† Free Gd^{3+} in the organs of living bodies may be a threat to the patients with impaired renal function, which may cause nephrogenic system fibrosis syndrome. To estimate the relative Gd^{3+} leakage of the PEGylated AuNR@SiO_2@$Gd_2O(CO_3)_2$ NAs, we dispersed them in PBS solutions and continuously stirred for 48 h at 37 °C. After filtrating the mixture solutions, we measured the concentration of the free Gd^{3+} utilizing ICP-MS. The obtained relative Gd^{3+} leakages of both DBNAs and CSNAs are close to 2.0×10^{-5}, which is negligible for clinically-used Gd-agents. In addition, we evaluated the intracellular toxicity, apoptosis, and proliferation using a normal human liver L-O2 cell line and the *in vivo* immunotoxicity in Balb/c mice (Fig. 5). Relative cell viabilities of normal L-O2 cells and carcinoma HeLa cells incubated with the DBNAs and CSNAs for 48 h were determined by the cell counting kit solution colorimetric assays. Fig. 5a shows that more than 90% of the normal liver L-O2 cells were alive and less than 10% of the cervical carcinoma HeLa cells were activated at a very high Gd^{3+} dosage of 200 μg L^{-1}, suggesting a negligible cytotoxicity of the synthesized NAs. Fig. 5b presents the data on the immunotoxicity and acute toxicity of the NAs injected into Balb/c mice.

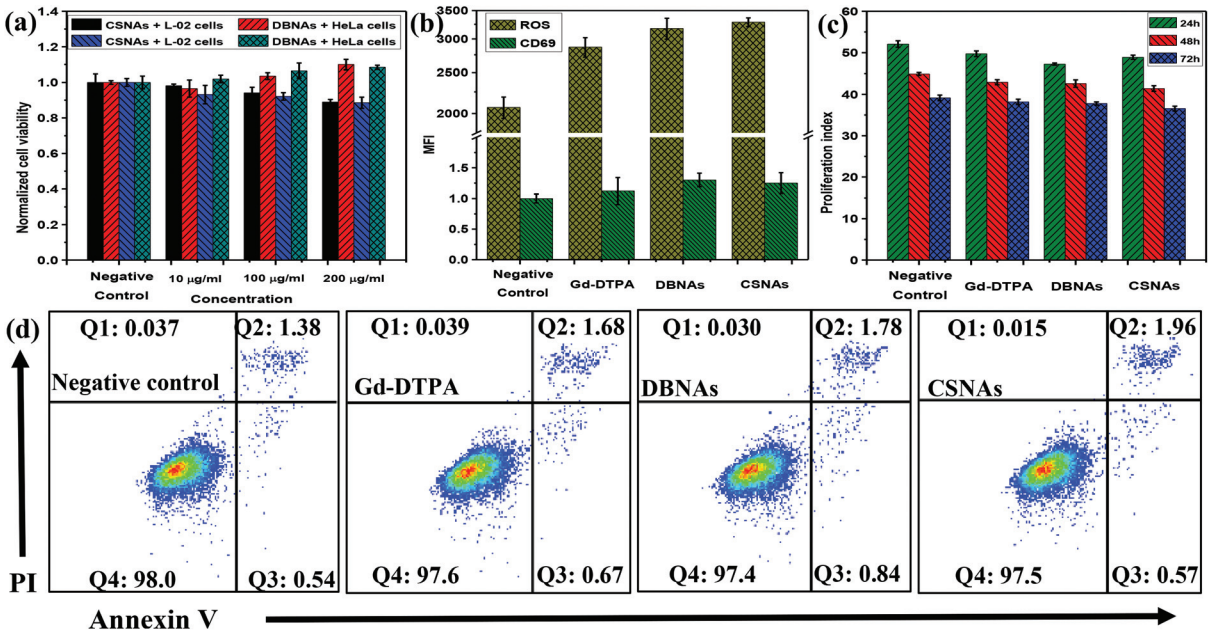

Fig. 5 (a) Normalized cell viability of the normal human liver L-O2 cells and cervical carcinoma HeLa cells after incubation with various concentrations of core–shell or dumbbell NAs for 48 h at 37 °C. (b) *In vivo* immunotoxicity data on the generation level of ROS on neutrophils and the expression level of CD69 on lymphocyte cells of peripheral blood measured by flow cytometry at 48 h after administration in Balb/c mice (21.7 mg kg^{-1}, mean ± SD, n = 5). (c) Proliferation index of L-O2 cells incubated with PBS, Gd-DTPA, DBNAs and CSNAs (10 μM) for 24, 48 and 72 h. (d) Apoptosis analysis of L-O2 cells measured by flow cytometry stained with Annexin-V/PI at the FL2-A channel for 48 h (mean ± SD, n = 3). Q1 is the region where cells should not turn up; Q2 represents the apoptosis or dead cells in the later period; Q3 represents the apoptosis cells in the early stage; Q4 displays the normal living cells.

No immunological reactions occurred and no obvious changes were observed in the generation level of ROS and the expression levels of CD69 on the negative control, clinical Gd-DTPA, the DBNAs and CSNAs, indicating an *in vivo* safety of the NAs in suitable dosages at a certain time. Furthermore, cell cycle analysis and apoptosis of L-O2 cells were assessed by flow cytometry stained with Annexin-V/PI (Fig. 5c and d and Fig. S23 and S24†), which discloses that both DBNAs and CSNAs have no influence on cell survival and possess a satisfactory biocompatibility in comparison with the negative control groups and commercial Gd-DTPA. However, more long-term nanotoxicity assays are necessitated to appraise their biomedical performances for practical utilization of these NAs in clinical administration.

Experimental

Materials and reagents

Gold(III) chloride trihydrate ($HAuCl_4 \cdot 3H_2O$, ≥49% Au basis), gadolinium nitrate hexahydrate ($Gd(NO_3)_3 \cdot 6H_2O$, 99.9%), silver nitrate ($AgNO_3$, ≥99.0%), sodium borohydride ($NaBH_4$, ≥98%), L-ascorbic acid (AA, ≥99.0%), ammonia hydroxide solution (NH_4OH, 28% NH_3 in H_2O, ≥99.99%) and hexadecyltrimethylammonium bromide (CTAB, ≥99%) were purchased from Sigma-Aldrich, United States. Tetraethyl orthosilicate (TEOS, ≥99.0%) was the product of China National Medicine Company. Urea (≥ 99.0%), ethanol (≥ 99.7%), hydrochloric acid (HCl, 35%–37%) and nitric acid (HNO_3, 69%–72%) were acquired from Guangzhou Chemical Reagent Factory. Agar (BR1200) and α,ω-dicarboxyl polyethylene glycol (HOOC-PEG-COOH, MW: 10 000) were purchased from Shanghai Yuanye Biological Science and Technologies Co. Ltd. Magnevist (Gd-DTPA) was obtained from Berlex Laboratories, Inc., USA. Fetal Bovine Serum (FBS), Dulbecco's Modified Eagle's Medium (DMEM) and Phosphate-Buffered Saline (PBS) were procured from Gibco, Switzerland. Cell Counting Kit-8 (CCK8) was provided by Dojindo Laboratories, Japan. Annexin V-FITC, Propidium Iodide (PI) and anti-mouse CD69-FITC were purchased from Becton Dickinson Pharmingen, USA. Deionized water used throughout all experiments was ultrapure Milli-Q water with an electrical resistivity of 18.25 MΩ cm (25 °C).

Characterization

TEM images and EDX spectra were recorded using a FEI Tecnai G2 Spirit instrument operating at 120 kV with a single tilt holder. HR-TEM, SAED, EELS-EFTEM, HAADF-STEM, EDX elemental mapping and line scanning were recorded on a Tecnai G2 F30 transmission electron microscope at an accelerating voltage of 300 kV. The TEM samples were prepared by drop-casting the synthesized nanocomposites dispersed in ethanol onto a carbon-coated 400-mesh Cu grids and evaporating the solvent overnight. The size distribution histograms of the nanoarchitectures were calculated by counting over 250

particles with Image-Pro Plus 5.0, and hydrodynamic size distributions were measured using the DLS method (EliteSizer, Brookhaven). XRD patterns were obtained on a D-MAX 2200× VPC using Cu-Kα radiation with a zero-background sample holder. The absorption spectra were recorded on a UV-visible-NIR spectrophotometer (UV-3150). FTIR spectra were measured using a Fourier transmission infrared spectrometer (EQUIN-OX 55) using a KBr pellet technique. High resolution XPS patterns were determined using an X-ray photoelectron spectrometer (ESCALab250, 26 kV). EPR data were collected on a Bruker EPR spectrometer (A300-10-12). Magnetization curves (*M–H*) at room temperature were acquired by using a magnetic property measurement system equipped with a superconducting quantum interference device (SQUID, Quantum Design). The Gd^{3+} ion concentrations of the samples were determined by ICP-MS (Optima 7300DV, PerkinElmer).

Synthesis of the monodisperse gold nanorods

Monodisperse AuNRs were synthesized *via* the well-known seed-mediated growth approach referred from the previously reported protocol with a slight modification. In this method, the seed solution was prepared by dissolving 0.364 g of CTAB in 8.34 mL of deionized water. Then 0.5 mL of $HAuCl_4$ (6 mM) and 1.16 mL of ice-cold $NaBH_4$ (10 mM) were added into the solution. After rapid stirring for 2 min, the mixture was maintained at 27 °C in a water bath for 2 h. To prepare the growth solution, 1.82 g of CTAB was dissolved in 42 mL of deionized water. Then 6 mL of $HAuCl_4$ and 1 mL of HCl (37%) were added into the solution. Subsequently 1.2–1.6 mL of ascorbic acid (50 mM) was added into the solution with stirring. In the meantime, the mixture turned from yellow to colorless. After performing the above procedures, 50 μL of seed solution prepared before was injected into the growth solution with gentle stirring for 10 s. Then the mixture was maintained in a 27 °C water bath for 12 h. Finally, the reaction products were collected by centrifugation at 7000 rpm for 30 min and then were dispersed in 25 mL of CTAB.

Encapsulation of gold nanorods with the silica

The silica encapsulating process was employed *via* a previously-reported Stöber method with some adjustments. After repeatedly washing and centrifuging (7000 rpm), 10 mL of selected pure samples diluted with 20 mL of deionized water was mixed with 0.2 mL of NH_4OH ultrasonically. During gentle stirring (60 rpm), 1 mL of TEOS alcohol solution was injected into the previous mixtures every 30 min for 2 h (4 times), and further stirred for 12 h. Then the sample was centrifuged and washed with alcohol and water alternately 2 times. The anisotropic dumbbell-like and core–shell AuNR@SiO_2 nanoarchitectures were formed in the presence and absence of 10 mg of CTAB in the mixture solution at the initial stage of the reaction. Before adding the CTAB, we purified gold nanorods by three cycles of dispersing them ultrasonically in NH_4NO_3 solution, hot acid ethanol and deionized water, respectively, followed by centrifugation.

Deposition with gadolinium oxide carbonate

The obtained precursors were repeatedly centrifuged at 8000 rpm for 8 min and washed ultrasonically at first. Then the sample was added into 50 mL of deionized water and mixed with 1 g of urea. Subsequently, 2 mL of $Gd(NO_3)_3{\cdot}6H_2O$ was added into the solution to maintain the molar ratio of Gd^{3+} as 0.2 mol L^{-1}. The mixture was stirred and heated in an 80 °C water bath for 3 h. 2 mmol of HOOC-PEG-COOH was added to the reaction solution and this was continuously stirred for 2 h. The collected sample was centrifuged at 8000 rpm for 8 min and washed with deionized water 4 times and with alcohol another 4 times, and then was dispersed in the deionized water or dried in a vacuum freeze drier to form powder samples. The prepared particles were denoted as PEGylated AuNR@SiO_2@$Gd_2O(CO_3)_2$ core–shell and dumbbell nanoarchitectures (CSNAs and DBNAs).

MRI *in vitro*

The longitudinal relaxation times of water protons in the presence of the NAs were measured using a MRI system (MicroMR-18, Shanghai Niumag Corp., 0.55 T). The NAs were ultrasonically dispersed in deionized water for 0.5 h at 40 °C. 0.2 mL of boiling agar solution (2.5 wt%) was rapidly injected into a 0.8 mL colloidal suspension placed in a 1.5 mL tube and was cooled down immediately to obtain a gel with 0.5 wt% agar. The gel in each tube possessed various Gd^{3+} concentrations of 0, 0.02, 0.04, 0.06, 0.08 mM, respectively. A commercially available Gd-DTPA gel, which is used as a clinical T_1 contrast agent, was prepared by the same way. Gel samples ensure that the coagulated particles keep a state of homogeneous dispersion in measurements. The parameters in the relaxation time measurement are as follows, IR series: P90 (μs) = 13.00, P180 (μs) = 26.00, TD = 961 720, SW (kHz) = 200, TR (ms) = 15 000, RGI = 20, RG2 = 3, NS = 2, DI (ms) = 1950, sampling number = 36. Longitudinal relaxivity (r_1) can be obtained by the linear fitting calculation of $1/T_1$ *versus* Gd^{3+} concentrations. Another 0.5 T MRI system (MesoMR23-60H-I, Shanghai TestNiumag Corp.) was adopted to obtain *in vitro* T_1-weighted MRI images. In this measurement, the samples with different Gd^{3+} amounts were directly dispersed in water without agar coagulating. The parameters in imaging are as follows, MSE series: FOV read = 100 mm, FOV phase = 100 mm, averages = 4, TR = 200 ms, TE = 18.2 ms, slices width = 4 mm.

MRI *in vivo*

An animal model of transplanted tumor on Balb/c nude mouse was used in the experiment. Animal experiments were conducted according to the National Institutes of Health guidelines on the rules of animal's research and the institution's animal board. Images were acquired by using a 1.5 T clinical MRI system (Siemens Medical Solutions, Erlangen, Germany). 100 μL PBS with 4T1 murine breast cancer cells (5×10^6) was subcutaneously administered into the back of each female Balb/c mouse (4–6 weeks old, around 20 g). After the

4T1 xenografted tumor grew to approximately 60 mm^2 for about 10 days, mice were anesthetized by intraperitoneal injection of 0.1% sodium pentobarbital (10 μL per g weight). Then the mice were administered with 10 μmol kg^{-1} of the NAs in 100 μL of PBS (2× buffer) *via* the tail vein and transported to the MRI scanner using a surface coil constructed specifically for small animals (3 inch in diameter). Scanning parameters: FOV = 64 mm, slice thickness = 2.0 mm, TR = 600 ms, TE = 12 ms, averages = 6.

Two-photon luminescence cell imaging

Human cervical carcinoma HeLa cells in the logarithmic growth phase were seeded on 24-well culture plates and then were cultured at 37 °C under 5% CO_2 overnight. The culture solution was replaced with a fresh culture solution containing 20 μg mL^{-1} samples for further 1 h incubation at the same environment. The media containing the excess NAs were removed. Cells washed with PBS were then fixed and observed by using a confocal laser scanning microscope (Leica TCS SP8 X) equipped with a femtosecond Ti-sapphire oscillator. The irradiation light for two-photon laser imaging was set at a wavelength of 800 nm. The living cell images were observed with a 620–700 nm band pass filter.

Photothermal heating measurements

The preliminary PTT experiments were conducted with a laser irradiating the solutions firstly. The aqueous PBS solutions (100 μL) containing PEGylated dumbbell or core–shell NAs (0.1 μmol L^{-1} Au) were irradiated with a 800 nm continuous laser at a power density of 1.0 W cm^{-2} for 10 min. The temperature rise was recorded every minute utilizing a thermocouple. Each test was conducted in triplicate. For further investigating the NIR-induced photothermal effect on cell ablation *in vitro*, the CCK8-based viability in cell culture media was determined by incubating the carcinoma HeLa cells in culture media including the NAs and exposing the samples to an 800 nm laser illumination. The HeLa cell culture protocol was the same as previously described in TPL cell imaging assays. The cells treated with the culture media with 100 μg L^{-1} NAs were irradiated for 2, 4, 6, 8, 10 min exposure times at 1.0 W cm^{-2}. Relative cell viabilities were determined using the standard CCK8 assays detailed in the following cytotoxicity assay.

Cytotoxicity assays

The CCK8 colorimetric method was employed to assess the cell viability levels of the NAs. The normal human liver L-O2 cells and cervical carcinoma HeLa cells were respectively seeded on 96-well culture plates (NEST Biotech. Co. Ltd, 701001) at a density of 8000 per well and cultured at 37 °C under 5% CO_2 in culture media involving DMEM + 10% FBS and 1640 + 10% FBS. After 24 h, the culture solutions were replaced with fresh media containing samples of different Gd^{3+} concentrations. After further incubation for 48 h, 10 μL of CCK-8 reagent was injected into each well. The cells with the sample or reagents were cultured for another 2 h at 37 °C under 5% CO_2. The absorbance of the living cells separated from the culture media was measured at 450 nm using a microplate reader (Multiskan MK3, Thermo Scientific) to obtain the final optical density values and the standard deviation values with three independent repetitions.

Immunotoxicity assays

Male BALB/c nude mice (6–8 weeks old, around 20 g) were purchased from the animal experiment center of Shanghai R&S Biotechnology Co., Ltd and maintained in the specific pathogen-free (SPF) environments during the time of the experiments. Twenty mice were divided into four groups at random: (1) PBS (100 μL, negative control), (2) Gd-DTPA (10 μmol kg^{-1}), (3) DBNAs (10 μmol kg^{-1}), (4) CSNAs (10 μmol kg^{-1}).

ROS assay of peripheral blood neutrophils. After removing the eyeballs of mice, 20 μL peripheral blood was obtained and mixed with 4 μL heparin sodium in a tube. 2 mL erythrocytes were added into the tube and stored in the dark for 2 min. 2 ml PBS was then added. The sample was centrifuged for 5 min at 1200 rpm. The ROS dye, H_2DCFDA, was added and its final concentration was 5×10^6 M. After storing in the dark for 20 min, the cells were resuspended with PBS and then analyzed by flow cytometry.

The expression of CD69 at T-lymphocyte in peripheral blood. The mice whose eyeballs were removed and peripheral blood was obtained were killed, and then their lymph nodes (at the jaw, clavicle, armpits, inguen and intestinal lineage) were isolated under sterile conditions. The membranes of lymph nodes were removed and ground using 200 mesh nylon. The cells were collected after filtration and washed with PBS, followed by the addition of 400 μL PBS for resuspension. The cells were stained in the dark for 30 min with anti-mouse CD69-PE and then analyzed by flow cytometry.

Cell cycle assays

The normal liver L-O2 cells in the logarithmic phase were digested with pancreatin and added to the culture media containing DMEM + 10%FBS + 1% Gln + 1% P/S. The cell suspension mixtures were seeded in 6 well culture plates (500 000 per well for cells) and grown at 37 °C under 5% CO_2. Then the samples with a concentration of 5 μM were added. The data were recorded after incubating cells for 24, 48, and 72 h. Cells were washed with 1 mL cold PBS and then separated *via* centrifugation at 1000 rpm for 5 min twice. 100 μL of cold PBS and 1 mL of cold 70% ethanol were added, evenly mixed and then stored at −20 °C overnight. Cells were washed with 1 ml PBS twice and centrifuged at 1000 rpm for 5 min. The supernatant was discarded and 400 μL cold PI solution containing RNase was added. After incubation for another 30 min at 4 °C in the dark, samples were detected by flow cytometry.

Apoptosis assays

The Annexin V-FITC/PI Apoptosis Detection Kit was used to assess the apoptosis of PEGylated AuNR@SiO_2@$Gd_2O(CO_3)_2$ NAs. 1×10^6 normal liver L-O2 cells were seeded on 12-well culture plates and then were cultured at 37 °C under 5% CO_2 for 24 h. Subsequently, they were incubated with PBS (negative

control), Gd-DTPA, core–shell and dumbbell NAs for further 48 h. Cells were collected by the trypsin digestion method and then washed with PBS twice. After the supernatant was decanted, cold 70% ethanol was added and the solution was gently shaken until cells were well dispersed and then incubated for 30 min at 20 °C. Ethanol was washed off by centrifugation twice with PBS. Cells were resuspended in 195 μL of PBS. Then, 5 μL of Annexin V-FITC was added and photophobically incubated for 10 min at room temperature. After washing with PBS twice, cells were resuspended and 10 μL of PI (20 μg mL^{-1}) was added. The apoptosis measurements were performed on a FACScan flow cytometer (Becton Dickinson, CA).

Conclusions

In summary, we have successfully prepared two multimodal nanoprobes with distinct core–shell and dumbbell heteroarchitectures *via* a controlling multistep synthetic strategy. The monodisperse and uniform nanoarchitectures (NAs) possess a controllable particle size and unique magnetic–plasmonic properties with high potential for *in vivo* applications. Based on the forming mechanism for two shapes of NAs, CTAB plays a key role as the structure-directing agent for the formation of anisotropic dumbbell structures; silica collapse and ensuing gadolinium reconstruction in the hot alkaline solution are validated as the underlying mechanism to hold the suitable particle size. *In vitro* MR images show that both NAs possess a larger longitudinal relaxivity and a better phantom imaging capability than that of clinical Gd-DTPA; *in vivo* MR images display a significant signal enhancement in imaging of mice tumors. In addition, the NAs exhibit a vivid two-photon cell imaging and striking photothermal conversion ability due to their superior plasmonic properties in the near-infrared regions. Compared with the conventional core–shell NAs, the intriguing dumbbell NAs present more excellent TPL and PTT abilities owing to their high intense SPR effect. *In vitro* cytotoxicity and *in vivo* immunotoxicity assays suggest both NAs are safe, biocompatible and have high potential for cancer imaging and therapy. Current research could shed new light on the integration of the magnetic–plasmonic nanosystem and blaze the trail to rationally design highly efficient nanoprobes with tunable sizes and anisotropic structures.

Acknowledgements

This work was funded by the National Natural Science Foundation of China (grant no. 11274394), the Fundamental Research Funds for the Central Universities (grant no. 11lgjc12), the Specialized Research Fund for the Doctoral Program of Higher Education (grant no. 20110171110023) and the Tianhe-2 supercomputing application cultivation projects (grant no. 74130-18823701). The authors would like to acknowledge Shanghai R&S Biotechnology Co., Ltd and Suzhou Niumag Analytical Instrument Corporation for their help in bioassays. Particularly, the authors are grateful to the Tianhe-2 National Super Computer Center in Guangzhou for financial support in material design and simulation.

References

1 X. Yang, M. Yang, B. Pang, M. Vara and Y. Xia, *Chem. Rev.*, 2015, **115**, 10410–10488.
2 H. Chen, L. shao, Q. Li and J. Wang, *Chem. Soc. Rev.*, 2013, **42**, 2679–2724.
3 A. Liu, G. Wang, F. Wang and Y. Zhang, *Coord. Chem. Rev.*, 2017, **336**, 28–42.
4 A. M. Smith, M. C. Mancini and S. Nie, *Nat. Nanotechnol.*, 2009, **4**, 710–711.
5 A. M. Alkilany, L. B. Thmopson, S. P. Boulos, P. N. Sisco and C. J. Murphy, *Adv. Drug Delivery Rev.*, 2012, **64**, 190–199.
6 Y. Chen, Y. Xianyu and X. Jiang, *Acc. Chem. Res.*, 2017, **50**, 310–319.
7 M. A. Muhammed, M. Döblinger and J. Rodríguez-Fernández, *J. Am. Chem. Soc.*, 2015, **137**, 11666–11677.
8 N. Wang, Z. Zhao, Y. Lv, H. Fan, H. Bai, H. Meng, Y. Long, T. Fu, X. Zhang and W. Tan, *Nano Res.*, 2014, **7**, 1291–1301.
9 L. Huang, L. Ao, D. Hu, W. Wang, Z. Sheng and W. Su, *Chem. Mater.*, 2016, **28**, 5896–5904.
10 D.-E. Lee, H. Koo, I.-C. Sun, J. H. Ryu, K. Kim and I. C. Kwon, *Chem. Soc. Rev.*, 2012, **41**, 2656–2672.
11 P. Hemmer, *Science*, 2013, **339**, 529–530.
12 C. S. Wood and M. M. Stevens, *Nature*, 2016, **539**, 505–506.
13 X. Lim, *Nat. News*, 2016, **531**, 26–28.
14 P. Verwilst, S. Park, B. Yoon and J. S. Kim, *Chem. Soc. Rev.*, 2015, **44**, 1791–1806.
15 L. Zhou, Z. Gu, X. Liu, W. Yin, G. Tian, L. Yan, S. Jin, W. Ren, G. Xing, W. Li, X. Chang, Z. Hu and Y. Zhao, *J. Chem. Mater.*, 2012, **22**, 966–974.
16 H. Koo, M. S. Huh, J. H. Ryu, D.-E. Lee, I.-C. Sun, K. Choi, K. Kim and I. C. Kwon, *Nano Today*, 2012, **6**, 204–220.
17 P. S. Patrick, J. Hammersley, L. Loizou, M. I. Kettunen, T. B. Rodrigues, D.-E. Hu, S.-S. Tee, R. Hesketh, S. K. Lyons, D. Soloviev, S. Amie, S. M. Fulton and K. M. Brindle, *Proc. Natl. Acad. Sci. U. S. A.*, 2014, **111**, 415–420.
18 R. J. McDonald, J. S. McDonald, D. F. Kallmes, M. E. Jentoft, D. L. Murray, K. R. Thielen, E. E. Williamson and L. J. Eckel, *Radiology*, 2015, **275**, 772–781.
19 M. Cho, R. Sethi, J. S. Narayanan, S. S. Lee, D. N. Benoit, N. Taheri, P. Decuzzi and V. L. Colvin, *Nanoscale*, 2014, **6**, 13637–13645.
20 Y. Shao, X. Tian, W. Hu, Y. Zhang, H. Liu, H. He, Y. Shen, F. Xie and L. Li, *Biomaterials*, 2012, **33**, 6438–6446.
21 M. Kircher, A. Zerda, J. V. Jokerst, C. L. Zavaleta, P. J. Kempen, E. Mittra, K. Pitter, R. Huang, C. Campos, F. Habte, *et al.*, *Nat. Med.*, 2012, **18**, 829–834.
22 T. Zhao, K. Yu, L. Li, T. Zhang, Z. Guan, N. Gao, P. Yuan, S. Li, S. Yao, Q.-H. Xu and G. Q. Xu, *ACS Appl. Mater. Interfaces*, 2014, **6**, 2700–2708.

23 X. He, J. Gao, S. S. Gambhir and Z. Cheng, *Trends Mol. Med.*, 2010, **16**, 574–583.
24 M. R. Ali, T. Han, X. Zhang, H. Xiao, Y. Tang, R. Wu, F. M. Fernández and M. A. El-Sayed, *J. Am. Chem. Soc.*, 2016, **138**, 15434–15442.
25 S.-S. Huang, S.-C. Wei, H.-T. Chang, H.-J. Lin and C.-C. Huang, *J. Controlled Release*, 2016, **221**, 9–17.
26 V. Amendola, S. Scaramuzza, L. Litti, M. Meneghetti, G. Zuccolotto, A. Rosato, E. Nicolato, P. Marzola, G. Fracasso, C. Anselmi, M. Pinto and M. Colombatti, *Small*, 2014, **10**, 2476–2486.
27 T. Wolfe, D. Chatterjee, J. Lee, J. D. Grant, S. Bhattarai, R. Tailor, G. Goodrich, P. Nicolucci and S. Krishnan, *Nanomed. Nanotechnol. Biol. Med.*, 2015, **11**, 1277–1283.
28 Q. Jia, J. Ge, W. Liu, S. Liu, G. Niu, L. Guo, H. Zhang and P. Wang, *Nanoscale*, 2016, **8**, 13067–13077.
29 L. Moriggi, C. Cannizzo, E. Dumas, C. R. Mayer, A. Ulianov and L. Helm, *J. Am. Chem. Soc.*, 2009, **131**, 10828–10829.
30 J. Wang, J. Liu, Y. Liu, L. Wang, M. Cao, Y. Ji, X. Wu, Y. Xu, B. Bai, C. Chen and Y. Zhao, *Adv. Mater.*, 2016, **28**, 8950–8958.
31 B. D. Yadav and V. Kumar, *Appl. Phys. Lett.*, 2010, **97**, 133701.
32 X. Tian, Y. Shao, H. He, H. Liu, Y. Shen, W. Huang and L. Li, *Nanoscale*, 2013, **5**, 3322–3329.
33 H. Wang, S. Zhang, X. Tian, C. Liu, L. Zhang, W. Hu, Y. Shao and L. Li, *Sci. Rep.*, 2016, **6**, 34367.
34 J. Choi, J.-H. Lee, T. H. Shin, H.-T. Song, E. Y. Kim and J. Cheon, *J. Am. Chem. Soc.*, 2010, **132**, 11015–11017.
35 J. Yin, C. Li, Y. Yang, W. Hu, H. Liu and Y. Shao, *RSC Adv.*, 2016, **6**, 72836–72844.
36 J. Yin, C. Li, D. Chen, J. Yang, H. Liu, W. Hu and Y. Shao, *Phys. Chem. Chem. Phys.*, 2017, **19**, 5366–5376.
37 D. K. Song, I. W. Lenggoro, Y. Hayashi, K. Okuyama and S. S. Kim, *Langmuir*, 2005, **21**, 10375–10382.
38 G. C. Albert, M. Roumeliotis and J. J. Carson, *Nanotechnology*, 2009, **20**, 505502.
39 J. Song, X. Yang, O. Jacobson, P. Huang, X. Sun, L. Lin, X. Yan, G. Niu, Q. Ma and X. Chen, *Adv. Mater.*, 2015, **27**, 4910–4917.
40 Y. Liu, M. Yang, J. Zhang, X. Zhi, C. Li, C. Zhang, F. Pan, K. Wang, Y. Yang, J. M. Fuentea and D. Cui, *ACS Nano*, 2016, **10**, 2375–2385.
41 J. Conde, N. Oliva, Y. Zhang and N. Artzi, *Nat. Mater.*, 2016, **15**, 1128–1138.
42 Z. Popovic, W. Liu, V. P. Chauhan, J. Lee, C. Wong, A. B. Greytak, N. Insin, D. G. Nocera, D. Fukumura, R. K. Jain and M. G. Bawendi, *Angew. Chem., Int. Ed.*, 2010, **122**, 8831–8834.
43 J. B. Ledeuil, A. Uhart, S. Soulé, J. Allouche, J. C. Dupin and H. Martinez, *Nanoscale*, 2014, **6**, 11130–11140.
44 R. Guillet-Nicolas, J.-L. Bridot, Y. Seo, M.-A. Fortin and F. Kleitz, *Adv. Funct. Mater.*, 2011, **21**, 4653–4662.
45 R. Guillet-Nicolas, M. Laprise-Pelletier, M. M. Nair, P. Chevallier, J. Lagueux, Y. Gossuin, S. Laurent, F. Kleitz and M.-A. Fortin, *Nanoscale*, 2013, **5**, 11499–11511.
46 J. Baltrusaitis, C. R. Usher and V. H. Grassian, *Phys. Chem. Chem. Phys.*, 2007, **9**, 3011–3024.
47 M. P. Casaletto, A. Longo, A. Martorana, A. Prestianni and A. M. Venezia, *Surf. Interface Anal.*, 2006, **38**, 215–218.
48 S. Hou, X. Hu, T. Wen, W. Liu and X. Wu, *Adv. Mater.*, 2013, **25**, 3857–3862.
49 J. Y. Park, M. J. Baek, E. S. Choi, S. Woo, J. H. Kim, T. J. Kim, J. C. Jung, K. S. Chae, Y. Chang and G. H. Lee, *ACS Nano*, 2009, **3**, 3663–3669.
50 C. Frangville, M. Gallois, Y. Li, H. H. Nguyen, N. L. Viguerie, D. R. Talham, C. Mingotaud and J.-D. Marty, *Nanoscale*, 2016, **8**, 4252–4259.
51 C. M. Hessel, V. P. Pattani, M. Rasch, M. G. Panthani, B. Koo, J. W. Tunnell and B. A. Korgel, *Nano Lett.*, 2011, **11**, 2560–2566.
52 M. H. Swat, G. L. Thomas, J. M. Belmonte, A. Shirinifard, D. Hmeljak and J. A. Glazier, *Methods Cell Biol.*, 2012, **110**, 325–366.
53 N. Savage, *Nature*, 2012, **491**, 62–63.